A Pressure Poisson Equation-Based Second-Order Method for Solving Moving Contact Line Problems with Topological Changes

Shuqing Chai[a,b], Zhilin Li[c], Zhen Zhang[a,d,*], Zhiwen Zhang[b]

[a] *Department of Mathematics, Guangdong Provincial Key Laboratory of Computational Science and Material Design, Southern University of Science and Technology (SUSTech), Shenzhen 518055, P.R. China.*
[b] *Department of Mathematics, The University of Hong Kong, Pokfulam Road, Hong Kong SAR, P.R. China.*
[c] *Center for Research in Scientific Computation (CRSC) and Department of Mathematics, North Carolina State University, Raleigh, NC 27695, USA*
[d] *International Center for Mathematics, National Center for Applied Mathematics (Shenzhen), Southern University of Science and Technology, Shenzhen 518055, P. R. China*

Abstract

We develop a second-order Cartesian grid based numerical method to solve moving contact line problems, which are modeled by the incompressible Navier-Stokes equations with the Navier-slip condition and the contact angle condition (CAC). The solutions of the flow field and the interface motion are decoupled in an alternating way. For a given interface, the velocity field is solved via a pressure Poisson equation formulation of the incompressible Navier-Stokes equations, which is numerically discretized by the immersed interface method. Once the velocity field is obtained, the interfacial kinematics together with the CAC is reformulated into a variational system, which is solved by the parametric finite element method (FEM). With this hybrid method, we detect topological changes in the interface by the inconsistency of neighboring normal vectors, which are directly computed through the parametric FEM. Second-order accuracy of the proposed method in both the interface and the contact line positions before and after topological changes has numerically validated. Moreover, with the help of the numerical method, the merging and collision dynamics of droplets on the substrates are easily investigated.

Keywords:
moving contact lines, topological changes, immersed interface method, parametric finite element method, pressure Poisson equation

1. Introduction

When two immiscible fluids are in contact with a solid substrate, a contact line is formed at the intersection of the fluid-fluid interface and the substrate. Contact lines are ubiquitous in nature and daily life, for example, water drops standing on a lotus leaf, coffee rings, and rainfall splashing on an umbrella. Investigation of contact line dynamics helps promote many industrial

*Corresponding author.
Email addresses: chaisq@hku.hk (Shuqing Chai), zhilin@math.ncsu.edu (Zhilin Li), zhangz@sustech.edu.cn (Zhen Zhang), zhangzw@hku.hk (Zhiwen Zhang)

processes, such as coating and inkjet printing [1, 2]. In comparison with experimental studies, numerical simulation of contact line dynamics has become a more and more popular tool due to the increasing computational power and the low cost for realization. Efficient and accurate numerical methods are in high demand in the simulation of moving contact line (MCL) problems with complex morphological changes.

Consider a two-dimensional MCL problem (see Figure 1). We model the fluid dynamics in the domain Ω_i $(i = 1, 2)$ by the incompressible Navier-Stokes equations (NSEs) , together with the stress force balancing conditions on the interface Γ, and the slip condition on the solid substrate Γ_s:

$$\rho\left(\frac{\partial \mathbf{u}}{\partial t} + \mathbf{u}\cdot\nabla\mathbf{u}\right) = -\nabla p + \nabla\cdot\mathbf{T}_i, \quad \text{in } \Omega_i, \tag{1}$$

$$\nabla\cdot\mathbf{u} = 0, \quad \text{in } \Omega_i, \tag{2}$$

$$\mathbf{n}\cdot[-p\mathbf{I} + \mathbf{T}_i]\cdot\mathbf{n} = -\gamma\kappa, \quad \mathbf{n}\cdot[\mathbf{T}_i]\cdot\boldsymbol{\tau} = 0, \quad [\mathbf{u}] = 0, \quad \text{on } \Gamma, \tag{3}$$

$$\boldsymbol{\tau}\cdot\mathbf{T}_i\cdot\mathbf{n} = -\beta_i\mathbf{u}_s, \quad \mathbf{u}\cdot\mathbf{n} = 0, \quad \text{on } \Gamma_s. \tag{4}$$

Here ρ is the density, $\mathbf{u} = (u, v)^\top$ and p are the velocity field and the pressure, and $\mathbf{T}_i$ is the Newtonian viscous stress tensor

$$\mathbf{T}_i = \mu_i\left(\nabla\mathbf{u} + (\nabla\mathbf{u})^\top\right).$$

μ_i $(i = 1, 2)$ is the viscosity of fluid in Ω_i. We assume ρ is constant throughout this paper.

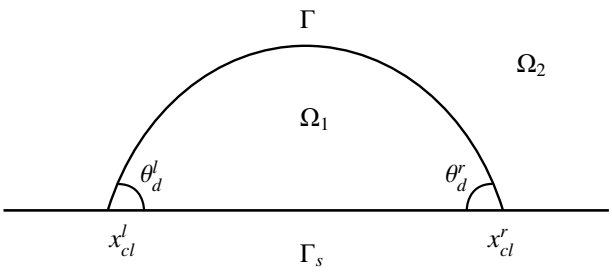

Figure 1: The moving contact line problem.

Equations in (3) provide the interfacial conditions on the interface Γ: the normal stress is balanced by the pressure jump and surface tension, while the tangential stress is continuous. The continuity condition is imposed for the velocity across the interface Γ. Here γ is the surface tension coefficient, κ is the curvature of interface, $\mathbf{n}$ and $\boldsymbol{\tau}$ are the normal and tangent unit vectors, and $[\cdot]$ denotes the jump across the interface from Ω_1 to Ω_2, i.e., $[\mathbf{T}_i] = \mathbf{T}_2 - \mathbf{T}_1$.

In classical fluid mechanics, the conventional no-slip condition, which imposes that a fluid in contact with a substrate moves with the velocity of the substrate, is used on Γ_s. However, when this condition is used in modeling two-phase flows with MCLs, an infinite rate of energy dissipation can be generated at the contact line [3, 4], which is non-physical and is known as the contact line singularity. There have been many pioneer works for alleviating this difficulty [5, 6, 7, 8, 9, 10]. In this paper, we adopt the Navier-slip boundary condition (NBC) on the solid substrate Γ_s, which is the first condition in (4). The second condition (4) is the no-penetration condition. Here $\mathbf{u}_s$ is the slip velocity of the fluid, and β_i $(i = 1, 2)$ are friction coefficients between each fluid and the solid substrate.

When the contact line is in equilibrium, the static contact angle θ_y (called Young's angle) between the fluid-fluid interface Γ and the solid substrate Γ_s, satisfies the Young-Dupré equation [11]:

$$\gamma \cos \theta_y = \gamma_2 - \gamma_1.$$

The equation describes the balance between the fluid-fluid interface tension γ and the two fluid-solid surface tensions γ_i along the tangential direction of Γ_s. A mismatch between the forces in this equation can lead to an unbalanced Young's force and thus a contact line motion. Motivated by [8, 9], we adopt the contact angle condition (CAC) for the contact line velocity u_{cl}:

$$\gamma \left(\cos \theta_d - \cos \theta_y \right) = -\beta_{cl} u_{cl}, \tag{5}$$

where β_{cl} is the friction coefficient between the interface and the substrate, and θ_d is the dynamic contact angle as shown in Figure 1.

The interface evolution satisfies the kinematic condition

$$\frac{\partial \mathbf{X}}{\partial t} \cdot \mathbf{n} = \mathbf{u}\left(\mathbf{X}, t\right) \cdot \mathbf{n}, \tag{6}$$

where $\mathbf{X}$ is the Eulerian coordinates of the interface Γ. This condition imposes that the interface moves with the same velocity as the local fluid, and is consistent with the continuity condition of the velocity field in (3).

Multiphase flow and moving contact line problems belong to a class of free boundary problems, where there are two main numerical challenges. The first challenge is how to efficiently and accurately solve the global fluid dynamics in the presence of moving interfaces, e.g., the bulk equations (1)-(2) and the interfacial conditions (3)-(4). The second numerical challenge is on the accurate tracking of an interface with complex morphological changes, e.g., large deformation and topological changes. In recent years, various works have been dedicated to tackling each of the challenges.

Concerning the first challenge, commonly used methods include (1) finite element methods (FEM) with body-fitted meshes [12, 13]; (2) FEM with unfitted meshes, e.g., the extended FEM and the immersed FEM [14, 15, 16, 17]; (3) Cartesian grid-based finite difference (FD) methods, e.g., the immersed boundary method, the immersed interface method (IIM) and the ghost fluid method [18, 19, 20, 21, 22, 23, 24]; (4) the boundary integral and boundary element method [25, 26, 27]. In general, the FD methods are easier to be implemented with fast solvers and will be the focus of the current work.

For the second issue, the interface tracking methods basically lie in two categories. The first category consists of Eulerian capturing methods, in which a scalar function is introduced to implicitly represent the interface. These include the level set methods [28, 29, 30], the volume-of-fluid methods [31, 32, 33], and the phase-field method [34, 8]. The second category comprises Lagrangian tracking methods, among which the most commonly used ones are the front tracking methods [35, 36, 37, 38]. Due to the implicit representation of the interface in Eulerian capturing methods, extra effort for the interface reconstruction based on the scalar function is needed. In addition, Eulerian capturing methods might introduce numerical dissipation and can be less accurate and less efficient in terms of both interface representation and evolution [39, 40]. In Lagrangian tracking methods, the mesh structure is usually ordered which makes it inconvenient to tackle topological changes, especially when a moving contact line is present. Moreover, careful re-meshing is required to maintain the equidistribution of the interface mesh in order to preserve

accuracy. In order to avoid the re-meshing, the parametric FEM was developed to equidistribute the mesh points in the long-time sense [41, 42]. Due to its variational framework, the parametric FEM can be easily applied to many variational problems, such as solid-state dewetting [43, 44] and two-phase flow [45]. It has been validated that the parametric FEM is second-order accurate in interface tracking [43, 44, 45].

To take the advantage of Cartesian grid-based methods in solving problems in irregular domains and explicit interface tracking methods in capturing interfacial dynamics, a hybrid IIM-parametric FEM was proposed for MCL problems to simultaneously maintain second-order accuracy in the interface and the velocity field [46]. In this method, the solutions of the velocity field and the interface kinematics are decoupled in an alternating way, with the input/output of the IIM being the output/input of the parametric FEM in time-marching. The key idea is to match the error rate of the velocity field on the Eulerian grid and that of interface geometries (position, curvature) so that second-order accuracy in both the IIM and the parametric FEM can be preserved during time-marching. The proposed method is easy to implement and has been successfully applied to study wetting/dewetting dynamics. However, this method is developed only for the Stokes flow, while the inertia effect can be important in many real problems.

In this work, we aim to generalize the hybrid IIM-parametric FEM to the Navier-Stokes equations and investigate topological changes of interfaces. To this end, the incompressible NSEs are recast into a pressure Poisson equation (PPE) formulation, which is solved by the IIM for the velocity field when the interface is fixed. We derive appropriate jump conditions along the x- and y-directions which are used to modify the discretized scheme at irregular points nearby the interface. Once the velocity field is obtained through the modified scheme within second-order accuracy, we can update the interface geometries by parametric FEM in which the weak formulation of the interface kinematics and the CAC are discretized. Another contribution of the work is to equip the numerical method with the ability to automatically capture topological changes in the interface. We detect topological changes by the inconsistency of neighboring normal vectors on the interface, which are directly computed through parametric FEM. The hybrid method inherits the property of long-time mesh equidistribution from parametric FEM and is expected to preserve second-order accuracy before and after a topological change. By simulations of the merging and collision dynamics of droplets on the substrates, the proposed method demonstrates its effectiveness in dealing with topological changes with sufficient accuracy and shows its potential in more realistic applications.

This paper is organized as follows. We first introduce the dimensionless form of the MCL problem and the interfacial jump conditions in Section 2 based on the PPE formulation. Then the IIM scheme for the velocity field and the parametric FEM for the moving interface are presented in Section 3. Techniques for topology control are also delineated. In Section 4, we numerically validate second-order convergence of the velocity field and the interface. Simulations of contact line dynamics with topological changes are illustrated. We conclude in Section 5.

2. A PPE formulation and interfacial jump conditions

2.1. The dimensionless PPE formulation

To nondimensionalize (1)-(6), we define the dimensionless variables as

$$\mu_i^* = \frac{\mu_i}{\mu_1}, \quad \beta_i^* = \frac{\beta_i}{\beta_1}, \quad \gamma_i^* = \frac{\gamma_i}{\gamma}, \quad \beta_{cl}^* = \frac{\beta_{cl}}{\mu_1}, \quad \kappa^* = L\kappa, \quad \mathbf{x}^* = \frac{\mathbf{x}}{L},$$

$$\mathbf{u}^* = \frac{\mathbf{u}}{U}, \quad p^* = \frac{p}{\rho_1 U^2}, \quad t^* = \frac{t}{L/U}, \quad \lambda_i = \frac{\mu_i/\mu_1}{\beta_i/\beta_1},$$
$$Re = \frac{\rho_1 U L}{\mu_1}, \quad Ca = \frac{\mu_1 U}{\gamma}, \quad We = ReCa, \quad \ell_s = \frac{\mu_1}{\beta_1 L},$$

where L and U are the characteristic length and the characteristic speed of the system, Re, Ca, We, and ℓ_s are the Reynolds number, the Capillary number, the Weber number, and the slip length, respectively.

Using these dimensionless variables, we recast the NSEs (1)-(2) in the dimensionless form as

$$\rho\left(\frac{\partial \mathbf{u}}{\partial t} + (\mathbf{u}\cdot\nabla)\mathbf{u}\right) = -\nabla p + \frac{1}{Re}\nabla\cdot\mathbf{T}_i, \tag{7}$$
$$\nabla\cdot\mathbf{u} = 0. \tag{8}$$

The asterisk symbols ($*$) are omitted for simplicity.

The interface conditions (3) on Γ become

$$\mathbf{n}\cdot\left[-p\mathbf{I} + \frac{1}{Re}\mathbf{T}_i\right]\cdot\mathbf{n} = -\frac{1}{We}\kappa, \quad \mathbf{n}\cdot[\mathbf{T}_i]\cdot\boldsymbol{\tau} = 0, \quad [\mathbf{u}] = 0. \tag{9}$$

Assuming the friction coefficients are equal, i.e., $\beta_1 = \beta_2$, which implies $\lambda_1 = 1$ and $\lambda_2 = \mu_2^*$, we have the dimensionless NBC (4) on Γ_s:

$$\frac{\partial u}{\partial y} = \frac{1}{\lambda_i \ell_s}u, \quad v = 0. \tag{10}$$

The non-dimensional form of the CAC (5) is

$$\beta_{cl}^* Ca\frac{\mathrm{d}x_{cl}^l}{\mathrm{d}t} = \cos\theta_d^l - \cos\theta_y, \quad -\beta_{cl}^* Ca\frac{\mathrm{d}x_{cl}^r}{\mathrm{d}t} = \cos\theta_d^r - \cos\theta_y, \tag{11}$$

where x_{cl}^l and x_{cl}^r are the left and right contact points, and θ_d^l and θ_d^r are the left and right dynamic contact angles, as shown in Figure 1.

The kinematic condition (6) remains the same as

$$\frac{\partial \mathbf{X}}{\partial t}\cdot\mathbf{n} = \mathbf{u}(\mathbf{X}, t)\cdot\mathbf{n}. \tag{12}$$

A classical numerical method for solving the NSEs is the projection method. In the projection method, an intermediate velocity field is computed and then projected onto the divergence-free space, and the pressure is updated by solving a Poisson equation based on the Helmholtz decomposition [47, 48]. Another type of method is based on the PPE formulation, which consists of a Poisson equation for the pressure and Helmholtz equations for the velocity field. In these methods, proper boundary conditions for pressure have to be derived for the equivalence of the NSEs and the PPE [49]. The numerical method based on the PPE formulation has been shown to be stable under the standard CFL condition [50].

In this paper, we use the PPE formulation discussed in [51, 52]. By applying the divergence operator on (7), the incompressible NSEs (7)-(8) are rewritten as

$$\Delta p = -\rho\nabla\cdot(\mathbf{u}\cdot\nabla\mathbf{u}), \tag{13}$$

$$\frac{\mu_i}{Re}\Delta\mathbf{u} = \nabla p + \rho\left(\frac{\partial \mathbf{u}}{\partial t} + \mathbf{u}\cdot\nabla\mathbf{u}\right). \tag{14}$$

The entire problem is recast as the interface evolution (12) and the PPE (13)-(14) in the fluids Ω_i ($i = 1, 2$), with the interface condition (9) at Γ, the NBC (10), the CAC (11), and an initial condition

$$\mathbf{u}(\mathbf{x}, 0) = \mathbf{u}_0. \tag{15}$$

For the convenience of numerical tests, we impose a no-slip condition and a no-penetration condition for the velocity on the upper boundary, and periodic boundary conditions for both the velocity and the pressure on the left and right boundaries.

2.2. Derivation and coordinate transformation of the jump conditions

The jump conditions are derived by following our previous work [46] based on local coordinate systems. The only difference in the derivation comes from the presence of the material derivative in the NSE, which we will explain here.

Essentially, we have the property that the jump in the material derivative of velocity is zero,

$$\frac{\mathrm{d}}{\mathrm{d}t}[\mathbf{u}] = \left[\frac{\partial \mathbf{u}}{\partial t} + (\mathbf{u}\cdot\nabla)\mathbf{u}\right] = 0, \tag{16}$$

which is obtained by taking the time derivative of the third condition in (9). Taking the difference in the limits of the momentum equation (7) at the interface from each side yields

$$\rho\left[\frac{\partial \mathbf{u}}{\partial t} + (\mathbf{u}\cdot\nabla)\mathbf{u}\right] = -[\nabla p] + \frac{1}{Re}[\nabla\cdot\mathbf{T}_i] = 0, \tag{17}$$

where (16) is used. The second equality in (17) leads to the same jump conditions as in [46]. It should be noted that equation (17) no longer holds when the density ρ is not continuous across the interface.

We summarize the jump conditions across the interface Γ for the NSEs (7)-(8) or the equivalent PPE formulation (13)-(14) as follows

$$[p] = 2\frac{1}{Re}\left[\mu_i\frac{\partial \mathbf{u}}{\partial n}\cdot\mathbf{n}\right] + \frac{\kappa}{We}, \tag{18}$$

$$\left[\frac{\partial p}{\partial n}\right] = 2\frac{1}{Re}\left[\mu_i\frac{\partial^2 \mathbf{u}}{\partial s^2}\cdot\mathbf{n}\right] - 4\frac{\kappa}{Re}\left[\mu_i\frac{\partial \mathbf{u}}{\partial s}\cdot\boldsymbol{\tau}\right], \tag{19}$$

$$\left[\mu_i\frac{\partial \mathbf{u}}{\partial n}\cdot\boldsymbol{\tau}\right] + \left[\mu_i\frac{\partial \mathbf{u}}{\partial s}\cdot\mathbf{n}\right] = 0, \tag{20}$$

$$[\mathbf{u}] = 0, \tag{21}$$

where $\frac{\partial}{\partial n}$ and $\frac{\partial}{\partial s}$ are the normal and tangential derivatives respectively. Equations (18) and (20) are the results of interfacial force balance in the normal and tangential directions.

In the case of continuous viscosity, we have $\left[\mu_i\frac{\partial \mathbf{u}}{\partial s}\right] = 0$. By using the incompressibility condition (8), we obtain

$$\left[\mu_i\frac{\partial \mathbf{u}}{\partial n}\cdot\mathbf{n}\right] = 0, \quad 2\left[\mu_i\frac{\partial^2 \mathbf{u}}{\partial s^2}\cdot\mathbf{n}\right] - 4\kappa\left[\mu_i\frac{\partial \mathbf{u}}{\partial s}\cdot\boldsymbol{\tau}\right] = 0. \tag{22}$$

Then we recover the jump conditions for continuous viscosity as in [53]:

$$[p] = \frac{\kappa}{We}, \quad \left[\frac{\partial p}{\partial n}\right] = 0, \quad \left[\frac{\partial \mathbf{u}}{\partial n}\right] = 0, \quad [\mathbf{u}] = 0. \tag{23}$$

Remark. *To obtain* (19)*, we have used the NSEs* (7)-(8) *in the above derivations. The same jump condition can be derived from the PPE formulation* (13)-(14)*. By applying the divergence operator on* (14) *and taking the difference between the resulting equation and* (13)*, we obtain a heat equation for* $\nabla \cdot \mathbf{u}$*. With the boundary condition* $\nabla \cdot \mathbf{u} = 0$ *on* $\partial\Omega \cup \Gamma$*, which is necessary to the equivalence of the NSEs and the PPE formulation [49], and the initial condition* $\nabla \cdot \mathbf{u}_0 = 0$*, we can recover the divergence-free condition* (8)*. Thus* (19) *can be derived from* (14) *in local coordinates by following the same idea as in [46].*

Using the PPE formulation (13)-(14) with the incompressibility condition, we can derive the additional jump conditions as

$$\left[\frac{\partial^2 \mathbf{u}}{\partial n^2}\right] = Re\,[\nabla p], \quad \left[\frac{\partial^2 p}{\partial n^2}\right] = -\left[\frac{\partial^2 p}{\partial s^2}\right], \tag{24}$$

whose derivation can be found in Appendix A.

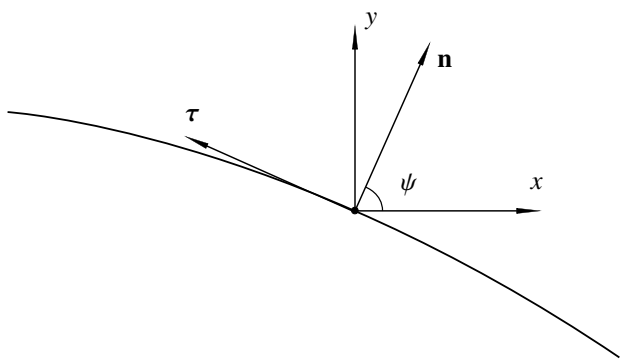

Figure 2: A local coordinate system.

As in [46], it is more convenient to express the jump conditions in terms of the x- and y-partial derivatives from the numerical perspective of MCL problems (also see Section 3.1). These can be done using local coordinate transformation. We introduce a local coordinate system whose origin is attached at a point on the interface Γ, with its axes in the normal and tangential directions of Γ (Figure 2). We denote the angle between the x-axis and the outward normal direction by ψ. Applying this coordinate transformation to the jump conditions (23)-(24), we obtain

$$\left[\frac{\partial^2 u}{\partial x^2}\right] = \frac{Re}{We}\left(-\sin\psi\cos^2\psi\frac{\partial\kappa}{\partial s}\right), \quad \left[\frac{\partial^2 u}{\partial y^2}\right] = \frac{Re}{We}\left(-\sin^3\psi\frac{\partial\kappa}{\partial s}\right), \tag{25}$$

$$\left[\frac{\partial^2 u}{\partial x\partial y}\right] = \frac{Re}{We}\left(-\sin^2\psi\cos\psi\frac{\partial\kappa}{\partial s}\right), \quad \left[\frac{\partial u}{\partial x}\right] = 0, \quad \left[\frac{\partial u}{\partial y}\right] = 0, \quad [u] = 0, \tag{26}$$

$$\left[\frac{\partial^2 v}{\partial x^2}\right] = \frac{Re}{We}\left(\cos^3\psi\frac{\partial\kappa}{\partial s}\right), \quad \left[\frac{\partial^2 v}{\partial y^2}\right] = \frac{Re}{We}\left(\sin^2\psi\cos\psi\frac{\partial\kappa}{\partial s}\right), \tag{27}$$

$$\left[\frac{\partial^2 v}{\partial x \partial y}\right] = \frac{Re}{We}\left(\sin\psi\cos^2\psi\frac{\partial\kappa}{\partial s}\right), \quad \left[\frac{\partial v}{\partial x}\right] = 0, \quad \left[\frac{\partial v}{\partial y}\right] = 0, \quad [v] = 0, \tag{28}$$

$$\left[\frac{\partial^2 p}{\partial x^2}\right] = \frac{1}{We}\left(-\cos 2\psi\frac{\partial^2\kappa}{\partial s^2}\right), \quad \left[\frac{\partial^2 p}{\partial y^2}\right] = \frac{1}{We}\left(\cos 2\psi\frac{\partial^2\kappa}{\partial s^2}\right), \tag{29}$$

$$\left[\frac{\partial^2 p}{\partial x \partial y}\right] = \frac{1}{We}\left(-\sin 2\psi\frac{\partial^2\kappa}{\partial s^2}\right), \tag{30}$$

$$\left[\frac{\partial p}{\partial x}\right] = \frac{1}{We}\left(-\sin\psi\frac{\partial\kappa}{\partial s}\right), \quad \left[\frac{\partial p}{\partial y}\right] = \frac{1}{We}\left(\cos\psi\frac{\partial\kappa}{\partial s}\right), \quad [p] = \frac{\kappa}{We}. \tag{31}$$

3. Numerical methods

In this section, we demonstrate numerical schemes to solve the MCL problem modeled by the NSEs. We first present the algorithm to solve for the velocity field based on the coupling system of the PPE (13)-(14) and the interface condition (9). Then we describe how to numerically solve for the interface motion and obtain the geometry information according to the kinematic condition (6) and the CAC (11). Furthermore, we elaborate on the techniques for tackling topological changes.

We partition the space with a Marker-and-Cell (MAC) staggered grid. The grid is uniform, i.e., $\Delta x = \Delta y = h$, where the grid points are $(x_i, y_j) = (ih, jh)$ for $i = 0, 1, 2, \cdots, N_x$ and $j = 0, 1, 2, \cdots, N_y$. The pressure p is located at the cell centers while the velocity fields $\mathbf{u}$ are at the midpoints of the vertical and horizontal cell edges, as shown in the left panel of Figure 3. Variables $u_{i,j}$, $v_{i,j}$, and $p_{i,j}$ are the approximations of the point values $u(x_i, y_{j+\frac{1}{2}})$, $v(x_{i+\frac{1}{2}}, y_j)$, and $p(x_{i+\frac{1}{2}}, y_{j+\frac{1}{2}})$ respectively, where $x_{i+\frac{1}{2}} = (i + \frac{1}{2})h$ and $y_{j+\frac{1}{2}} = (j + \frac{1}{2})h$. The grid points, at which p and $\mathbf{u}$ are located, are classified into regular and irregular points. When a standard five-point stencil for the discrete Laplacian operator is crossed by the interface, the central grid point is called an irregular point. Otherwise, it is a regular point. For example, $u_{i,j}$, $p_{i-1,j}$, and $p_{i,j}$ locate at irregular points in the right panel of Figure 3.

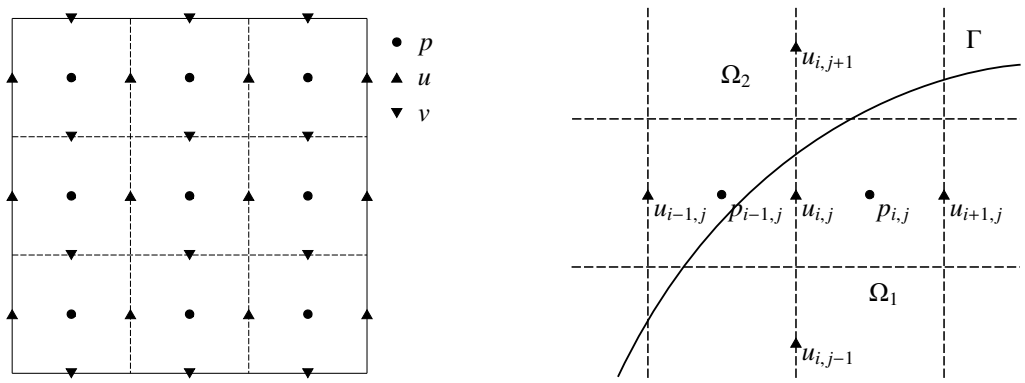

Figure 3: The left panel illustrates the MAC staggered grid. The right diagram is an example in which $u_{i,j}$ locates at an irregular point.

3.1. A modified pressure Poisson scheme

The PPE (13)-(14) formulation is equivalent to (7)-(8) in the continuous case. But in general they are not equivalent when spatially discretized due to the boundary conditions [50, 52, 54]. By projecting the velocity field onto the divergence-free space, we obtain the following numerical scheme: *Given the velocity field* $\mathbf{u}^n$ *and the interface* Γ^n*, find* $\mathbf{u}^{n+1}$ *and* p^{n+1} *s.t.*

$$\begin{cases} \Delta p^{n+1} = -\rho \nabla \cdot (\mathbf{u}^n \cdot \nabla \mathbf{u}^n), \quad \mathbf{x} \in \Omega_i, & (32a) \\ \left[p^{n+1}\right] = \dfrac{\kappa}{We}, \quad \left[\dfrac{\partial p^{n+1}}{\partial n}\right] = 0, \quad \text{on } \Gamma^n, & (32b) \end{cases}$$

$$\begin{cases} \dfrac{1}{Re}\Delta u^* - \dfrac{\rho}{\Delta t} u^* = \dfrac{\partial p^{n+1}}{\partial x} + \rho\left(-\dfrac{1}{\Delta t} u^n + (\mathbf{u}^n \cdot \nabla u^n)\right), \quad \mathbf{x} \in \Omega_i, & (33a) \\ [u^*] = 0, \quad \left[\dfrac{\partial u^*}{\partial n}\right] = 0, \quad \text{on } \Gamma^n, & (33b) \end{cases}$$

$$\begin{cases} \dfrac{1}{Re}\Delta v^* - \dfrac{\rho}{\Delta t} v^* = \dfrac{\partial p^{n+1}}{\partial y} + \rho\left(-\dfrac{1}{\Delta t} v^n + (\mathbf{u}^n \cdot \nabla v^n)\right), \quad \mathbf{x} \in \Omega_i, & (34a) \\ [v^*] = 0, \quad \left[\dfrac{\partial v^*}{\partial n}\right] = 0, \quad \text{on } \Gamma^n, & (34b) \end{cases}$$

$$\begin{cases} \Delta \psi^{n+1} = \dfrac{\nabla \cdot \mathbf{u}^*}{\Delta t}, \quad \mathbf{x} \in \Omega_i, & (35a) \\ \left[\psi^{n+1}\right] = 0, \quad \left[\dfrac{\partial \psi^{n+1}}{\partial n}\right] = 0, \quad \text{on } \Gamma^n, & (35b) \end{cases}$$

$$\mathbf{u}^{n+1} = \mathbf{u}^* - \Delta t \nabla \psi^{n+1}, \quad \mathbf{x} \in \Omega_i. \tag{36}$$

We first solve the pressure p^{n+1} and the velocity field $\mathbf{u}^*$ in (32)-(34) using the IIM. Note that (32)-(34) are three Poisson/Helmholtz equations of the pressure/velocity and form a closed system due to the jump condition $\left[\frac{\partial p^{n+1}}{\partial n}\right]$. To achieve second-order accuracy for both pressure and velocity, the three Poisson/Helmholtz equations have to be discretized with truncation errors being $O(h)$ at the irregular points and $O\left(h^2\right)$ at the regular points. To this end, we utilize the jumps in second derivatives (c.f. (24))

$$\left[\frac{\partial^2 p^{n+1}}{\partial n^2}\right] = -\left[\frac{\partial^2 p^{n+1}}{\partial s^2}\right], \quad \left[\frac{\partial^2 u^*}{\partial n^2}\right] = Re\left[\frac{\partial p^{n+1}}{\partial x}\right], \quad \left[\frac{\partial^2 v^*}{\partial n^2}\right] = Re\left[\frac{\partial p^{n+1}}{\partial y}\right],$$

and transform them into the form of the x- and y-partial derivatives (c.f.(25)-(31)). Then the correction terms for the pressure and the velocity field at irregular points are approximated within

$O\left(h^3\right)$ accuracy, e.g.,

$$
\begin{aligned}
p_{i,j}^{c,n+1} =& [p^{n+1}]_{\mathbf{X}^*} + (x_{i+\frac{1}{2}} - x^*)\left[\frac{\partial p^{n+1}}{\partial x}\right]_{\mathbf{X}^*} + (y_{j+\frac{1}{2}} - y^*)\left[\frac{\partial p^{n+1}}{\partial y}\right]_{\mathbf{X}^*} \\
&+ \frac{1}{2}\left((x_{i+\frac{1}{2}} - x^*)^2\left[\frac{\partial^2 p^{n+1}}{\partial x^2}\right]_{\mathbf{X}^*} + 2(x_{i+\frac{1}{2}} - x^*)(y_{j+\frac{1}{2}} - y^*)\left[\frac{\partial^2 p^{n+1}}{\partial x \partial y}\right]_{\mathbf{X}^*}\right. \\
&\left. +(y_{j+\frac{1}{2}} - y^*)^2\left[\frac{\partial^2 p^{n+1}}{\partial y^2}\right]_{\mathbf{X}^*}\right),
\end{aligned} \tag{37}
$$

$$
\begin{aligned}
u_{i,j}^{c,*} =& [u^*]_{\mathbf{X}^*} + (x_i - x^*)\left[\frac{\partial u^*}{\partial x}\right]_{\mathbf{X}^*} + (y_{j+\frac{1}{2}} - y^*)\left[\frac{\partial u^*}{\partial y}\right]_{\mathbf{X}^*} \\
&+ \frac{1}{2}\left((x_i - x^*)^2\left[\frac{\partial^2 u^*}{\partial x^2}\right]_{\mathbf{X}^*} + 2(x_i - x^*)(y_{j+\frac{1}{2}} - y^*)\left[\frac{\partial^2 u^*}{\partial x \partial y}\right]_{\mathbf{X}^*}\right. \\
&\left. +(y_{j+\frac{1}{2}} - y^*)^2\left[\frac{\partial^2 u^*}{\partial y^2}\right]_{\mathbf{X}^*}\right),
\end{aligned} \tag{38}
$$

$$
\begin{aligned}
v_{i,j}^{c,*} =& [v^*]_{\mathbf{X}^*} + (x_{i+\frac{1}{2}} - x^*)\left[\frac{\partial v^*}{\partial x}\right]_{\mathbf{X}^*} + (y_j - y^*)\left[\frac{\partial v^*}{\partial y}\right]_{\mathbf{X}^*} \\
&+ \frac{1}{2}\left((x_{i+\frac{1}{2}} - x^*)^2\left[\frac{\partial^2 v^*}{\partial x^2}\right]_{\mathbf{X}^*} + 2(x_{i+\frac{1}{2}} - x^*)(y_j - y^*)\left[\frac{\partial^2 v^*}{\partial x \partial y}\right]_{\mathbf{X}^*}\right. \\
&\left. +(y_j - y^*)^2\left[\frac{\partial^2 v^*}{\partial y^2}\right]_{\mathbf{X}^*}\right),
\end{aligned} \tag{39}
$$

where $\mathbf{X}^*$ is chosen to be a point on the interface close to the irregular point and is not necessary to be the orthogonal projection of the grid point onto the interface. Furthermore, we obtain the correction terms for ψ as $\psi_{i,j}^{c,n+1} = 0$ by

$$
\left[\frac{\partial^2 \psi^{n+1}}{\partial n^2}\right] = \left[\frac{\nabla \cdot \mathbf{u}^*}{\Delta t}\right] = 0.
$$

Based on these correction terms, the discretized scheme for the PPE formulation with interface conditions (32)-(36) can be written as: *Given the velocity field* $\mathbf{u}^n$*, solve* $\mathbf{u}^{n+1}$ *and* p^{n+1} *from the following schemes*

$$
\Delta_h p^{n+1} = -\rho \nabla_h \cdot (\mathbf{u} \cdot \nabla_h \mathbf{u})^n + C_1, \quad \text{at } (x_{i+\frac{1}{2}}, y_{j+\frac{1}{2}}), \tag{40}
$$

$$
\frac{1}{Re}\Delta_h u^* - \frac{\rho}{\Delta t} u^* = D_h^x p^{n+1} + \rho\left(-\frac{1}{\Delta t} u^n + (\mathbf{u} \cdot \nabla_h u)^n\right) + C_2, \quad \text{at } (x_i, y_{j+\frac{1}{2}}), \tag{41}
$$

$$
\frac{1}{Re}\Delta_h v^* - \frac{\rho}{\Delta t} v^* = D_h^y p^{n+1} + \rho\left(-\frac{1}{\Delta t} v^n + (\mathbf{u} \cdot \nabla_h v)^n\right) + C_3, \quad \text{at } (x_{i+\frac{1}{2}}, y_j), \tag{42}
$$

$$
\Delta_h \psi^{n+1} = \frac{\nabla_h \cdot \mathbf{u}^*}{\Delta t} + C_4, \quad \text{at } (x_{i+\frac{1}{2}}, y_{j+\frac{1}{2}}), \tag{43}
$$

$$
\mathbf{u}^{n+1} = \mathbf{u}^* - \Delta t \nabla_h \psi^{n+1}, \quad \text{at } (x_i, y_{j+\frac{1}{2}}) \text{ and } (x_{i+\frac{1}{2}}, y_j), \tag{44}
$$

where

$$
\nabla_h \cdot (\mathbf{u} \cdot \nabla_h \mathbf{u})^n = \left(D_h^x u^n\right)^2 + (D_h^y v^n)^2 + 2(D_h^x v^n)(D_h^y u^n), \tag{45}
$$

$$(\mathbf{u}\cdot\nabla_h u)^n = D_h^x\left(u^n\right)^2 + D_h^y\left(u^n v^n\right), \quad (\mathbf{u}\cdot\nabla_h v)^n = D_h^x\left(u^n v^n\right) + D_h^y\left(v^n\right)^2. \tag{46}$$

Equalities (45) and (46) hold when $\nabla_h \cdot \mathbf{u}^n = 0$. In above expressions, the operators Δ_h, ∇_h, $\nabla_h\cdot$, D_h^x, and D_h^y are the standard second-order central difference operators.

In (40)-(44), the correction terms C_1, C_2, C_3, and C_4 are nonzero only at the irregular points:

$$C_1 = \begin{cases} -C\left\{\Delta_h p^{n+1}\right\} - \rho C\left\{\nabla_h\cdot(\mathbf{u}\cdot\nabla_h\mathbf{u})^n\right\}, & \text{at irregular points,} \\ 0, & \text{at regular points,} \end{cases} \tag{47}$$

$$C_2 = \begin{cases} -\frac{1}{Re}C\left\{\Delta_h u^*\right\} + C\left\{D_h^x p^{n+1}\right\} + \rho C\left\{(\mathbf{u}\cdot\nabla_h u)^n\right\}, & \text{at irregular points,} \\ 0, & \text{at regular points,} \end{cases} \tag{48}$$

$$C_3 = \begin{cases} -\frac{1}{Re}C\left\{\Delta_h v^*\right\} + C\left\{D_h^y p^{n+1}\right\} + \rho C\left\{(\mathbf{u}\cdot\nabla_h v)^n\right\}, & \text{at irregular points,} \\ 0, & \text{at regular points,} \end{cases} \tag{49}$$

$$C_4 = \begin{cases} \frac{1}{\Delta t}C\left\{\nabla_h\cdot\mathbf{u}^*\right\}, & \text{at irregular points,} \\ 0, & \text{at regular points,} \end{cases} \tag{50}$$

The correction terms $C\{\cdot\}$ can be directly computed. For example, for the irregular point as in the right panel of Figure 3, we explicitly write the correction term

$$C\{\Delta_h u^*(x_i, y_{j+\frac{1}{2}})\} = -\frac{u_{i-1,j}^{c,*}}{h^2} - \frac{u_{i,j+1}^{c,*}}{h^2},$$

where $u_{i-1,j}^{c,*}$ and $u_{i,j+1}^{c,*}$ are defined in a similar manner as in (38).

To discretize the NBC (10) on the bottom substrate, we need to introduce a ghost value $u_{i,-1}$ at the ghost point $(x_i, y_{-\frac{1}{2}})$. Then the standard finite difference scheme can be applied at the regular boundary point:

$$\frac{u_{i,-1} + u_{i,0}}{2} = \lambda_i l_s \frac{u_{i,0} - u_{i,-1}}{h}. \tag{51}$$

At the irregular boundary point near the contact points, correction terms can be similarly defined so that (51) is also used with a correction term.

Following [52], we can approximate local pressure boundary conditions using

$$\frac{\partial p}{\partial y} = \frac{2}{Re}\left(\frac{v_{i,1}}{h^2} + \frac{D_h^x u}{h}\right) \quad \text{at } (x_{i+\frac{1}{2}}, 0) \quad \text{and} \quad \frac{\partial p}{\partial y} = \frac{2}{Reh^2}v_{i,N_y-1} \quad \text{at } (x_{i+\frac{1}{2}}, y_{N_y}).$$

The same scheme is also applied to ψ on the boundary. It has been shown that these treatments lead to second-order accuracy in the pressure field [52].

3.2. Interface evolution and the moving contact line

For the evolution of the interface $\mathbf{X}(s,t)$, we can rewrite the kinematic condition (12) with the definition of the curvature as

$$\frac{\partial \mathbf{X}}{\partial t}\cdot\mathbf{n} = \mathbf{U}\cdot\mathbf{n}, \tag{52}$$

$$\kappa\mathbf{n} = \frac{\partial^2\mathbf{X}}{\partial s^2}, \tag{53}$$

where s is the arclength, and $\mathbf{U} = \mathbf{u}|_\Gamma$ is the velocity on the interface.

We parametrize the interface $\mathbf{X}$ with $\rho \in \mathbb{I} := [0, 1]$. We use clockwise parameterization for our convenience, where $\rho = 0, 1$ correspond to the left and right contact points respectively. Then the arclength is $s(\rho, t) = \int_0^\rho |\frac{\partial \mathbf{X}}{\partial \rho}| \mathrm{d}\rho$ and $\frac{\partial s}{\partial \rho} = |\frac{\partial \mathbf{X}}{\partial \rho}|$. Define the function spaces for the curvature and the interface position respectively as

$$\mathbb{K} := H^1(\mathbb{I}), \quad \mathbb{X} := \left\{ \mathbf{g} = (g_1, g_2)^\top \in \left(H^1(\mathbb{I})\right)^2 : g_2(0) = g_2(1) = 0 \right\},$$

where $H^1(\mathbb{I})$ is the standard Sobolev space. The L^2 inner product on the interface is defined as

$$(f, g)_\Gamma = \int_{\Gamma(t)} f(s) \cdot g(s) \mathrm{d}s = \int_{\mathbb{I}} f(s(\rho, t)) \cdot g(s(\rho, t)) \left| \frac{\partial \mathbf{X}}{\partial \rho} \right| \mathrm{d}\rho.$$

Taking inner products of (52) with $\phi \in \mathbb{K}$ and (53) with $\mathbf{g} \in \mathbb{X}$ on the interface, and applying integration by parts, we obtain the interface evolution equations in the weak form

$$\left(\frac{\partial \mathbf{X}}{\partial t} \cdot \mathbf{n}, \phi \right)_\Gamma - (\mathbf{U} \cdot \mathbf{n}, \phi)_\Gamma = 0, \ \forall \phi \in \mathbb{K}, \tag{54}$$

$$(\kappa \mathbf{n}, \mathbf{g})_\Gamma + \left(\frac{\partial \mathbf{X}}{\partial s}, \frac{\partial \mathbf{g}}{\partial s} \right)_\Gamma - \left(\frac{\partial x}{\partial s} \cdot g_1 \right) \Big|_{\rho=0}^{\rho=1} = 0, \ \forall \mathbf{g} \in \mathbb{X}, \tag{55}$$

where $\frac{\partial \mathbf{X}}{\partial s} = \frac{\partial \mathbf{X}/\partial \rho}{|\partial \mathbf{X}/\partial \rho|}$. With the CAC (11), noticing that $\cos \theta_d^l = \frac{\partial x}{\partial s}\Big|_{\rho=0}$, $\cos \theta_d^r = \frac{\partial x}{\partial s}\Big|_{\rho=1}$, equation (55) is reduced to

$$(\kappa \mathbf{n}, \mathbf{g})_\Gamma + \left(\frac{\partial \mathbf{X}}{\partial s}, \frac{\partial \mathbf{g}}{\partial s} \right)_\Gamma - \left(\cos \theta_y \cdot g_1 \right) \Big|_{\rho=0}^{\rho=1} + \beta_{cl}^* Ca \left(\frac{\mathrm{d}x_{cl}^l}{\mathrm{d}t} g_1(0) + \frac{\mathrm{d}x_{cl}^r}{\mathrm{d}t} g_1(1) \right) = 0.$$

To apply the parametric FEM, decompose the parameter space $\mathbb{I} = \cup_{k=1}^K \mathbb{I}_k$ with $\mathbb{I}_k = [\rho_{k-1}, \rho_k]$, and define the finite element spaces to approximate $\mathbb{K}$ and $\mathbb{X}$ respectively as

$$\mathbb{K}^h := \{ \phi \in C(\mathbb{I}) : \phi|_{\mathbb{I}_k} \in P_1, k = 1, 2, \cdots, K \} \subset \mathbb{K},$$
$$\mathbb{X}^h := \left\{ \mathbf{g} \in (C(\mathbb{I}))^2 : g_2(0) = g_2(1) = 0 \right\} \subset \mathbb{X},$$

where P_1 denotes all polynomials with degrees at most one. The time domain is uniformly partitioned as $[0, T] = \cup_{m=1}^M [t_{m-1}, t_m]$, where $t_m = m\tau$ with $\tau = T/M$. The velocity of the interface $\mathbf{U}^m$ is interpolated from the velocity field on the grid $\mathbf{u}^m$. Let $\mathbf{X}^m$, $\mathbf{n}^m$, and κ^m be the numerical approximations of the interface $\mathbf{X}$, the unit normal vector $\mathbf{n}$, and the curvature κ at time t_m respectively. Then numerical scheme to approximate the interface evolution (52)-(53) is written as: *Given* $\mathbf{X}^m$, $\mathbf{n}^m$, *and* $\mathbf{U}^m$, *find* $\mathbf{X}^{m+1} \in \mathbb{X}^h$ *and* $\kappa^{m+1} \in \mathbb{K}^h$ *s.t.*

$$\left(\frac{\mathbf{X}^{m+1} - \mathbf{X}^m}{\tau} \cdot \mathbf{n}^m, \phi \right)_{\Gamma^m} - (\mathbf{U}^m \cdot \mathbf{n}^m, \phi)_{\Gamma^m} = 0, \ \forall \phi \in \mathbb{K}^h, \tag{56}$$

$$\begin{aligned} &\left(\kappa^{m+1} \mathbf{n}^m, \mathbf{g} \right)_{\Gamma^m} + \left(\frac{\partial \mathbf{X}^{m+1}}{\partial s}, \frac{\partial \mathbf{g}}{\partial s} \right)_{\Gamma^m} - \left(\cos \theta_y \cdot g_1 \right) \Big|_{\rho=0}^{\rho=1} \\ &+ \beta_{cl}^* Ca \left(\frac{x_l^{m+1} - x_l^m}{\tau} g_1(0) + \frac{x_r^{m+1} - x_r^m}{\tau} g_1(1) \right) = 0, \ \forall \mathbf{g} \in \mathbb{X}^h. \end{aligned} \tag{57}$$

3.3. Detection of Topological Changes

Topological changes often occur in complex multiphase flows, such as droplet merging and impact dynamics. Due to the implicit representation of interfaces, Eulerian capturing methods are usually used when handling topological changes. For instance, the level set method and its variants are among the most popular methods and can be especially accurate in some applications [55]. In Lagrangian tracking methods, where the interface is represented by connected markers, numerical modifications of the connectivity of the markers are needed when topological change events happen. Such complex and artificial "surgery" is often regarded as a disadvantage of the Lagrangian methods. In general, topological changes happen when two interfaces or two parts of one interface become closer and the distance between them is smaller than some physical threshold (usually characterized by the resolution of a continuum model, and sometimes can be approximated by the grid size) [35].

To encode this threshold and deal with topological changes automatically, a front-tracking method with an underlying grid was introduced in [36], in which the underlying grid is used to reconnect the interface after topological changes. One also needs to use Lagrangian information to detect topological changes. For example, Leung and Zhao proposed a meshless particle algorithm [39], in which the interface particles are corresponding to the Eulerian reference grid points in their neighborhoods and thus are quasi-uniformly distributed. The Lagrangian information, such as normal vectors and global parameterization, along with the underlying Eulerian grid is used to process topological changes.

We adopt a similar idea and use the Lagrangian information on each marker for local detection of topological change. The algorithm is outlined as follows:

Algorithm 1 Detection of topological change

1: **for** each marker **do**
2: denote the marker as $\mathbf{X}_0$ and its normal vector as $\mathbf{n}_0$;
3: collect the markers in its ϵ-neighborhood to get a set of markers $\mathbf{X}_i, i = 1, \ldots, k$, s.t. $\|\mathbf{X}_0 - \mathbf{X}_i\| < \epsilon$ and corresponding normal vectors $\mathbf{n}_i, i = 1, \ldots, k$;
4: compute the angles between the normal vectors, i.e., $\theta_i = \cos^{-1}(\mathbf{n}_0 \cdot \mathbf{n}_i)$;
5: a topological change occurs if any angle $\theta_i > \theta^{\perp}$.
6: **end for**

In Algorithm 1, a prescribed parameter ϵ is introduced as the sensing range within which topological changes can be perceived by the numerical algorithm. This parameter, as expected, can notably affect simulations and sometimes can sway the occurrence time of a topological change event. This is investigated through our numerical results and is discussed in detail in section 4.2. In this work, the parameter ϵ is prescribed in advance for each numerical example. To detect topological changes, we concentrate on the "ϵ-neighborhood" of each marker on the interface. To avoid markers on different segments of the interface tangling before a topological change is detected, we choose ϵ larger than the grid size. We consider a topological change occurring if there is local information inconsistency [39], i.e., the normal vectors at two neighboring markers are well separated with a large angle between them ($\theta_i > \theta^{\perp}$). Here $\theta^{\perp}$ is a degree measure of local information inconsistency and is fixed at $\theta^{\perp} = \frac{\pi}{2}$. Once the topological change is detected, other makers without inconsistent local information in their neighborhood are reconnected and are used to represent new interface(s).

Due to the use of parametric FEM, Algorithm 1 can be conducted conveniently with many

advantages. Firstly, due to the equidistribution property of the parametric FEM, the one-to-one correspondence between interface particles and Eulerian grid points in [39] is not necessary for achieving a quasi-uniform sampling. Thus the work of re-meshing and resampling at every step is avoided in our method. Moreover, the Lagrangian information, such as normal vectors, can be easily accessed from parametric FEM. Local reconstruction of the interface to acquire the Lagrangian information is avoided. With the help of the normal vectors, we are able to distinguish different pieces of interfaces from a local perspective.

In MCL problems, we mainly have to deal with the topological changes in terms of the formation and elimination of contact lines. When a piece of interface gets close to a substrate, two scenarios could happen locally in 2D:

- A droplet approaches a substrate, as shown in the left panel of Figure 4. The vapor between them is getting away as the interface is approaching the substrate. When the droplet touches the substrate, its interface would eventually breaks up and two new contact points are formed.

- A droplet sits on a substrate with its top approaching the substrate, as shown in the right panel of Figure 4. The droplet becomes thinner and longer so that it would be "pinched" into two.

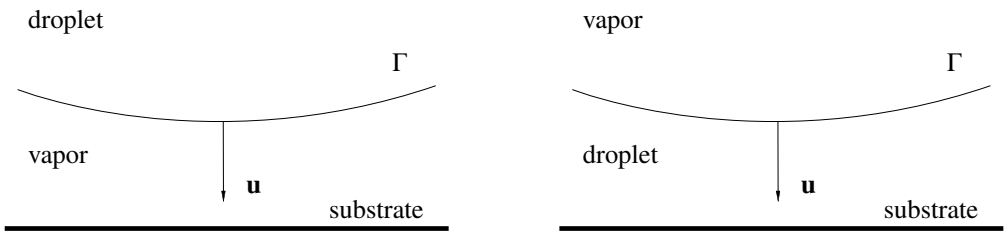

Figure 4: Two different scenarios when an interface approaches a substrate.

The physical mechanisms underlying topological changes are complicated and are still under investigation. In general, the first scenario is believed as a result of short-range attractive forces, while the second scenario is a result of Rayleigh instability due to surface tension [35]. Consider when the droplet is close to the substrate in the first scenario. The vapor film between the substrate and the droplet has a very small thickness, which reaches the order as the mean free path. In this case, the continuum model fails, and the Boltzmann equation should be used instead [56]. To limit our study within the scope of the continuum model, we introduce the small parameter ϵ as a threshold for the length scale, and the complex dynamics undergone within this length scale are ignored.

Reversely, when two contact lines come close, there are also two scenarios in 2D that may happen:

- The wet area between the contact points shrinks, as shown in the left panel of Figure 5. The droplet would gently rise and would be no longer in contact with the substrate.

- The dry area between the contact points diminishes, as shown in the right panel of Figure 5. Two droplets would eventually coalesce and the contact points vanish.

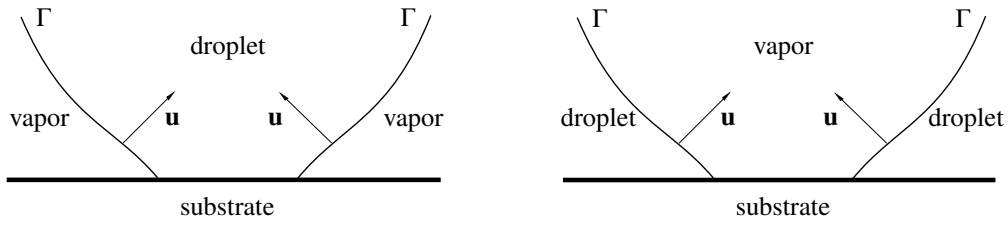

Figure 5: Two different scenarios when two contact points come close.

Our method is capable of dealing with changes in contact points by introducing a ghost interface Γ'. The ghost interface does not contribute to the dynamics but only helps detect topological changes. The ghost interface and the actual interface are axially symmetric about the substrate, as shown in Figure 6. With the help of the ghost interface, a scenario in which a contact point emerges or vanishes is similar to a topological change with closed interfaces. For example, the impact of a droplet onto a substrate can be treated as the coalescence of a droplet and the ghost one (left panel of Figure 6), while the motion of a droplet leaving a substrate can be treated as the split of a droplet and its ghost (right panel of Figure 6). Thus, concerning scenarios in Figure 4 and Figure 5, we can still apply Algorithm 1 to deal with the formation and elimination of contact lines as if they are parts of closed interfaces.

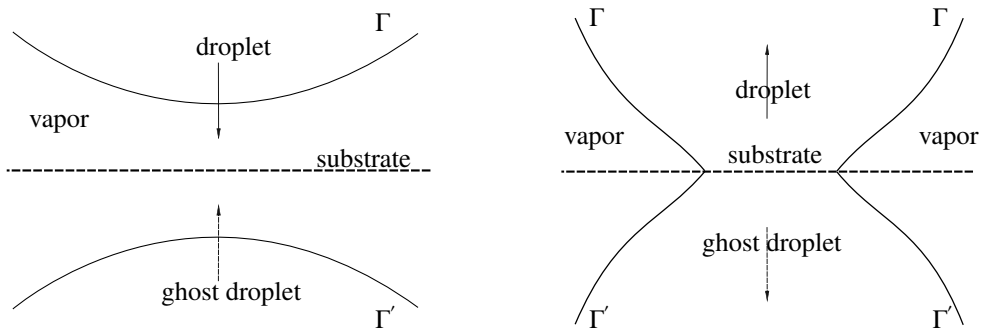

Figure 6: A droplet and its ghost with a ghost interface Γ'.

4. Numerical results

In this section, we present numerical studies on MCL problems modeled by Navier-Stokes equations. We first present the benchmark problem of droplet relaxation on a substrate as a convergence test. Then we examine the second-order accuracy-preserving property of the proposed method when a topological change happens in the next example of merging. Numerical simulations of merging and collision dynamics demonstrate that our method is capable of dealing with topological changes. In the following examples, we perform simulations on a staggered grid in $[0, 2]\times[0, 1]$. The dimensionless numbers including the Reynolds number, the Capillary number, the Weber number, and the slip length are $Re = 1$, $Ca = 0.1$, $We = 0.1$, and $\ell_s = 0.25$ respectively unless otherwise specified.

4.1. A convergence test

Example 1 *(Droplet relaxation).* For the convergence test, we study the relaxation of a droplet. The droplet is initially shaped as half of an ellipse and placed on a substrate, with Young's angle $\theta_y = \frac{\pi}{2}$. Driven by the unbalanced Young's force and surface tension, the droplet eventually relaxes to a semi-circular shape. The dynamic evolution of the interface is shown as the snapshots in Figure 7.

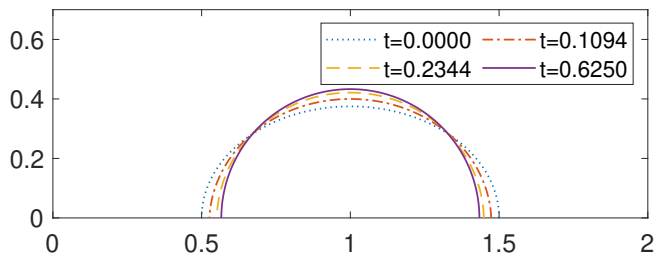

Figure 7: Snapshots of the droplet relaxation.

The computation is performed on different grids $N_x \times N_y = 32 \times 16, 64 \times 32, 128 \times 64, 256 \times 128, 512 \times 256$ and 1024×512. We choose the solution computed on the finest grid $N_x \times N_y = 1024 \times 512$ as the reference solution. To estimate the error of the interfaces, we denote the symmetric difference of two sets $A, B \in \mathbb{R}^2$ by

$$A \Delta B := (A \cup B) \backslash (A \cap B).$$

Using the symmetric difference, we define the error of the interfaces at t_m as

$$\|E_{\mathbf{X}}(t_m)\|_{sym} := \Upsilon\left(\Omega(\mathbf{X}^m) \Delta \Omega(\mathbf{X}^m_{ref})\right), \tag{58}$$

where $\Omega(\mathbf{X})$ denotes the fluid area enclosed by the interface $\mathbf{X}$, and $\Upsilon(A) = \int_A \mathrm{d}S$. We use $\mathbf{X}^m$ and $\mathbf{X}^m_{ref}$ to denote the interface position at time t_m, with the subscript ref representing the solution computed on the finest grid. The errors and the corresponding convergence rates at $t = 0.5$ are summarized in Table 1. The convergence rates of the velocity field, the pressure, the interface, and the contact lines achieve second order.

Our method inherits the long-time equidistribution property from the parametric FEM. By defining the mesh distribution function as [43, 46]

$$\Psi(t = t_m) = \Psi^m := \frac{\max_{1 \le k \le K} |\mathbf{X}^m(\rho_k) - \mathbf{X}^m(\rho_{k-1})|}{\min_{1 \le k \le K} |\mathbf{X}^m(\rho_k) - \mathbf{X}^m(\rho_{k-1})|}, \tag{59}$$

we can see that $\Psi(t_m)$ converges to 1 as $m \to \infty$ in Figure 8.

$N_x \times N_y$	$\|E_u\|_2$	rate$_u$	$\|E_v\|_2$	rate$_v$	$\|E_p\|_2$	rate$_p$
32×16	$1.0147e-02$	-	$6.1567e-03$	-	$5.5430e-01$	-
64×32	$2.2083e-03$	2.2000	$1.3355e-03$	2.2047	$7.7936e-02$	2.8303
128×64	$6.5530e-04$	1.7527	$3.9615e-04$	1.7533	$2.1957e-02$	1.8276
256×128	$1.7539e-04$	1.9016	$1.0680e-04$	1.8911	$6.8641e-03$	1.6776
512×256	$4.2979e-05$	2.0288	$2.4272e-05$	2.1375	$1.0775e-03$	2.6714

$N_x \times N_y$	$\|E_{\mathbf{X}}\|_{sym}$	rate$_{\mathbf{X}}$	$\|E_{cl}\|_\infty$	rate$_{cl}$
32×16	$1.9534e-02$	-	$7.3690e-03$	-
64×32	$2.7958e-03$	2.8047	$1.5716e-03$	2.2293
128×64	$6.3652e-04$	2.1350	$4.1450e-04$	1.9228
256×128	$1.6504e-04$	1.9474	$1.0676e-04$	1.9569
512×256	$3.1104e-05$	2.4076	$2.2882e-05$	2.2221

Table 1: Errors and convergence rates of velocity fields, pressure, interface, and contact lines. Absolute errors are computed by comparing with the reference solution computed on $N_x \times N_y = 1024 \times 512$. Errors E_u, E_v, E_p, $E_{\mathbf{X}}$, and E_{cl} denote the absolute errors of the velocity field u, v, the pressure p, the interface $\mathbf{X}$, and the contact line position x_{cl} respectively. Norms $\|\cdot\|_2$, $\|\cdot\|_\infty$, and $\|\cdot\|_{sym}$ denote l_2, l_∞, and symmetric norms respectively.

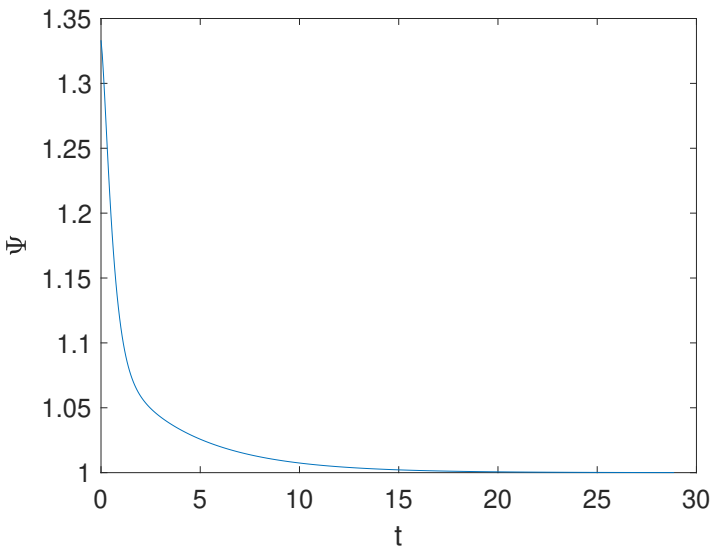

Figure 8: The temporal evolution of the mesh distribution function $\Psi(t)$.

We also measure the contact angles θ_d in equilibrium through a geometric formula [57]. In equilibrium states, given the chord length by the distance between two contact points $\hat{L} = X_r - X_l$ and the distance between the chord and the highest point of the arc $\hat{h} = \max\{Y_k\}$, the contact angle can be computed through the geometric formula $\tan\theta_d = \frac{\hat{h}\hat{L}}{(\hat{L}/2)^2 - \hat{h}^2}$. We find that the maximum

discrepancy between the measured contact angle θ_d and the specified contact angle θ_y is less than 1°, which also demonstrates the accuracy of our method.

4.2. Simulations of topological changes

Example 2 *(Merging)*. Next, we present an example of the merging of two droplets on a substrate with Young's angle $\theta_y = \frac{\pi}{3}$. Two semi-circularly shaped droplets are initially placed apart from each other at a distance of 0.07 between their closest contact points. As Young's angle $\theta_y = \frac{\pi}{3}$ is smaller than the initial contact angles $\theta_d = \frac{\pi}{2}$, the two droplets spread, and eventually, touch with each other and coalesce.

The errors $\|E_{\mathbf{X}}\|_{sym}$ and $\|E_{cl}\|_\infty$ are computed in this example as the grid is refined. Figure 9 shows the errors at $t = 2.5$ after the coalescence of the two droplets. An approximately second-order convergence rate is observed in the log-log plot, which demonstrates a good accuracy-preserving property of our method when dealing with topological changes.

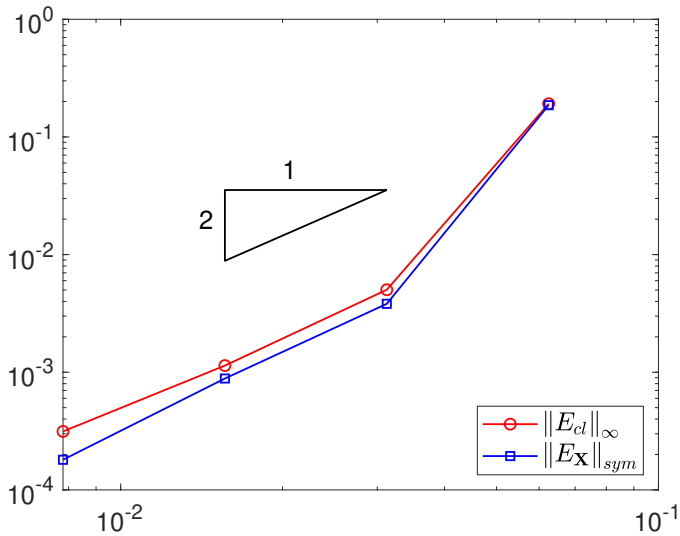

Figure 9: The errors of the interface and the contact lines after merging are shown in the log-log plot.

We investigate the merging dynamics of droplets at different Reynolds numbers. Driven by the unbalanced Young's forces, the two droplets start to spread independently on the substrate. The contact points of the two droplets are then getting closer and eventually meet, which results in the merging of the two droplets. The merging processes are shown in terms of the snapshots at $t = 0.125$ in the upper panel ($Re = 1$) and at $t = 0.25$ in the lower panel ($Re = 100$) in Figure 10. When they begin to merge at their edges, the two interfaces coalesce into one and the resulting interface continues to evolve towards a new circular arc according to the curvature force. It is remarkable that the difference in Reynolds numbers can affect not only the merging time, but also the amount of deformation after merging. In the case with a larger Reynolds number ($Re = 100$), the merging occurs later and more deformations of the interfaces are observed before and after merging. The oscillated shape of the coalesced interface is also observed in [58].

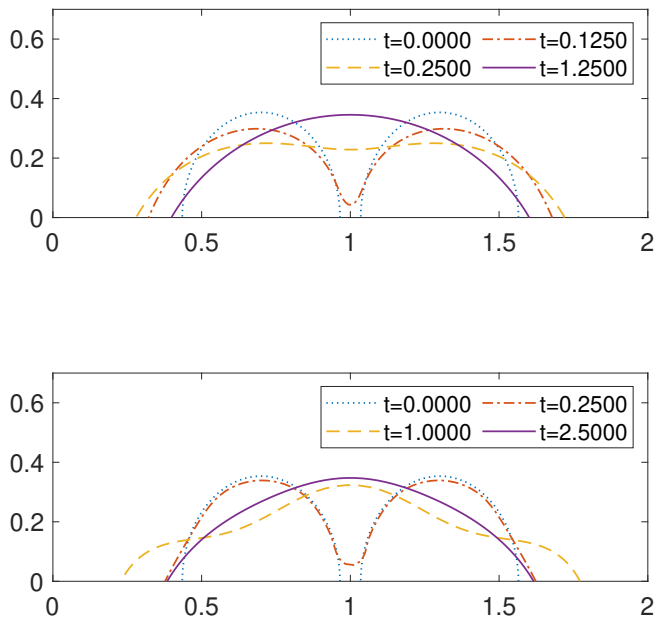

Figure 10: Merging dynamics at different Reynolds numbers. The snapshots of interface profiles are shown at different times. The case with $Re = 1$ is shown in the upper panel and the case with $Re = 100$ is shown in the lower panel.

Next, we place two droplets at different distances from each other. The initial distance between their closest contact points is changed from 0.07 in Figure 10 to 0.23 in Figure 11. As expected, the merging phenomenon is observed in the case of large Reynolds number (the lower panel of Figure 11, $Re = 100$) but not in the case of small Reynolds number (the upper panel of Figure 11, $Re = 1$). The stronger inertia helps accelerate the motion of the interfaces and thus promotes the merging of the droplets. The simulation results mimic the merging of inkjet droplets in the printing process, in which the nozzle is positioned appropriately so that the merging or not can be controlled. This may indicate a potential application of the proposed method in simulations of such industrial problems.

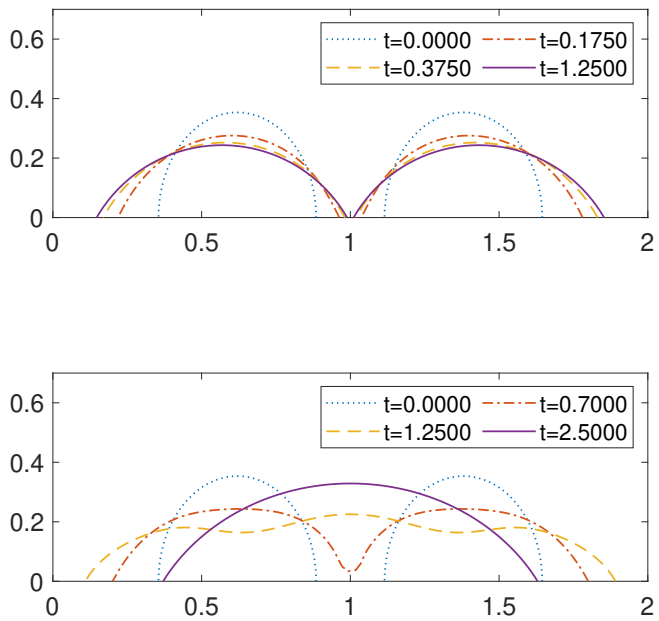

Figure 11: The effect of Reynolds numbers on the occurrence of merging. Shown are the interface dynamics in the cases with $Re = 1$ (upper panel) and $Re = 100$ (lower panel).

Example 3 *(Collision).* We investigate the impact dynamics of a droplet on a substrate. A circular-shaped droplet is placed above the substrate with a downward initial velocity of 7 while the background fluid is at rest.

First, we consider the influence of different Reynolds numbers. The Young's angle is set at $\theta_y = \frac{\pi}{2}$. As shown in Figure 12, the droplet falls down and hits the substrate, with its bottom in contact with the substrate. Two contact points are formed and the closed interface becomes an open one. In the process, the first topological change event occurs, corresponding to the first scenario of Figure 4. After the collision, a velocity field pointing to side parts is generated and the droplet spreads rapidly. In the case of a smaller Reynolds number $Re = 50$ (upper panel), the capillary force begins to dominate and drives the interface towards a semi-circular shape as its equilibrium profile. However, for a larger Reynolds number $Re = 100$ (lower panel), the stronger inertia gives rise to a larger velocity field and the droplet pinches off from its middle part. This leads to a second topological change, as illustrated in the second scenario of Figure 4. The droplet splits into two smaller ones. Then these two small drops continue their motions following contact line dynamics until their equilibrium states are reached.

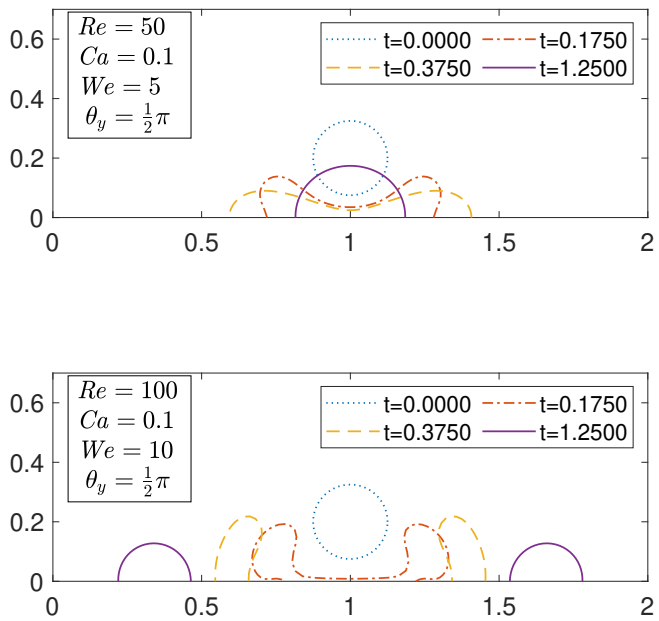

Figure 12: Collision and pinch-off at different Reynolds numbers, $Re = 50$ in the upper panel and $Re = 100$ in the lower panel.

Next, we investigate the impact dynamics by modifying the Reynolds number, the Capillary number, and the Young's angle. We collect the numerical results in Figure 13. In comparison with Figure 12, if the capillary effect is strengthened with a smaller $Ca = 0.02$ (first panel in Figure 13), the deformation of the interface is severely reduced after the collision and the droplet relaxes to its equilibrium state much faster. No pinch-off is observed in this case. To study more interesting phenomena, we choose a hydrophobic substrate with a larger Young's angle $\theta_y = \frac{3}{4}\pi$ which significantly enriches the dynamics of droplets after collisions. The breakup of droplets is also observed in the case of a moderate Capillary number $Ca = 0.1$ (second panel), but the split droplets recoil their interfaces and eventually stand on the substrate with the contact angle at nearly $\frac{3}{4}\pi$. At a small Capillary number $Ca = 0.02$ (third panel), the droplet no longer breaks up but instead rebounds after the collision. This is a result of the strong capillary force and the hydrophobicity of the substrate, which intend to maintain the droplet shape with a small energy loss. Furthermore, if the inertia is stronger with $Re = 150$ (fourth panel), the droplet breaks up into two and each new drop bounces off the substrate. This corresponds to the splashing phenomenon.

In our numerical investigations of topological change events, the threshold parameter ϵ plays a very important role. Therefore it is necessary to study the influence of ϵ. In general, topological change events can usually be detected based on some temporal or spatial indicators, as illustrated in [35]. These are two aspects in the description of topological change events and are typically related to each other. However, specifying rupture time as a temporal indicator requires prior

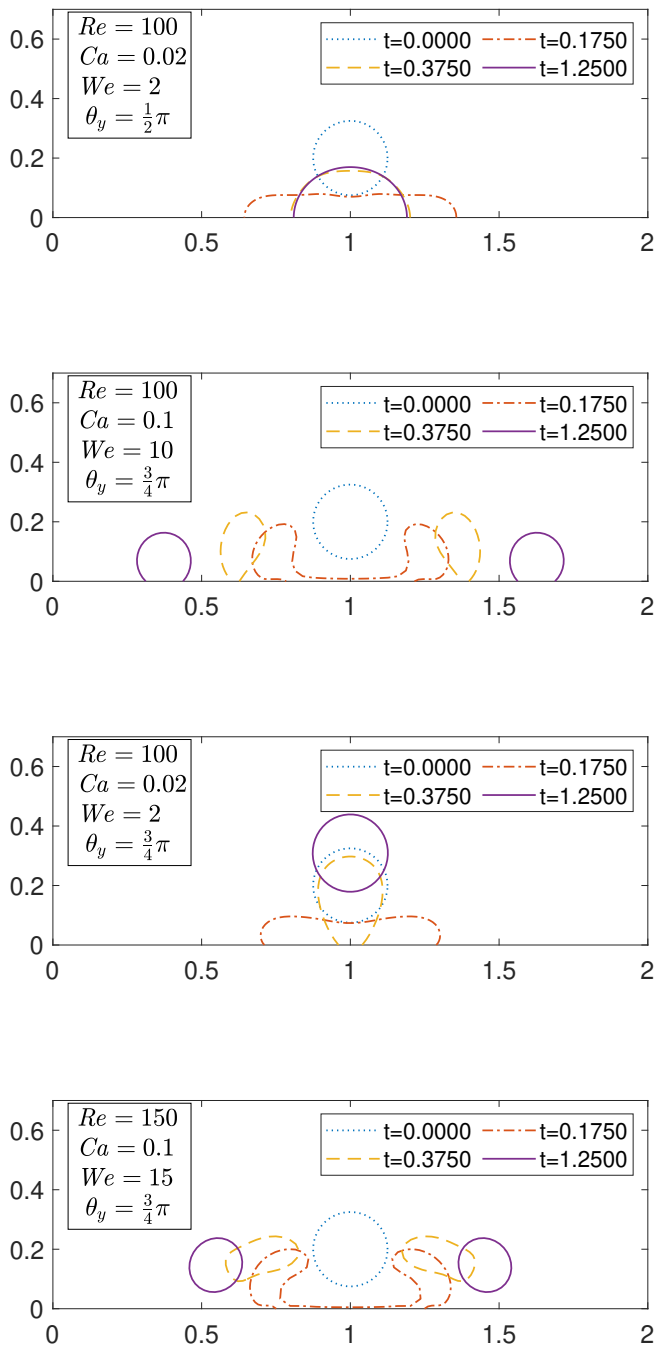

Figure 13: Collision and pinch-off at different settings.

knowledge of the solution, which makes it a less general approach. The threshold parameter ϵ in our method is a spatial indicator that also affects the occurrence time of topological change events. This effect is worth studying.

To this end, we consider the droplet collision event on the substrate with $Re = 50$ (shown in Figure 12). We focus on the collision time at which the closed droplet interface touches the substrate and two new contact points are formed. For different $\epsilon \in [0.0078, 0.0195]$ (twice to five times the grid size), we record the collision times detected by our numerical method. As shown in Figure 14, the collision time is not quite sensitive for larger ϵ. However, as ϵ becomes smaller as twice the grid size, the collision time increases significantly. This may attribute to the slow motion of the bottom part of the droplet when it gets closer to the substrate, and the complex multiscale mechanism in contact line dynamics may come into play. We also present the volume change in the droplet after the collision for different choices of ϵ in Figure 14. Small volume change is observed for small ϵ, and increasing ϵ definitely leads to larger volume change. Fortunately, the total scale of the volume change is acceptable. This numerical study may suggest that taking ϵ as three times the grid size is optimal since at this value the collision time is not swayed too much while the volume change is also small.

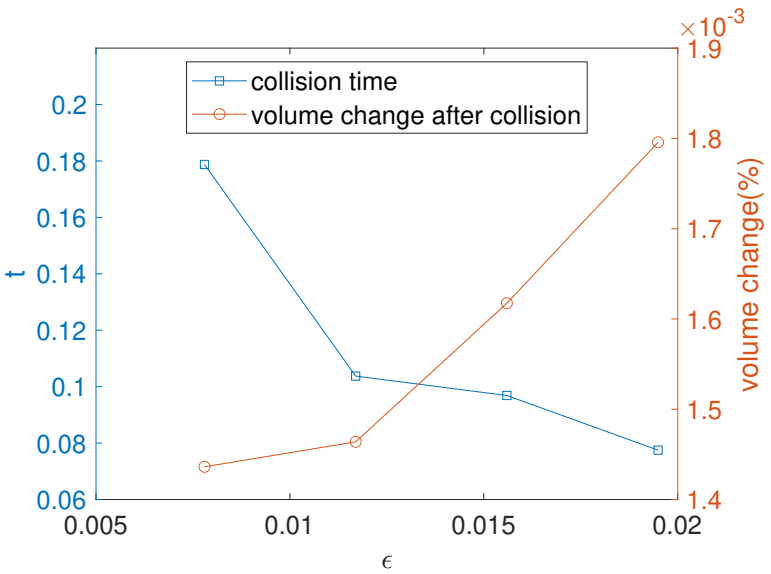

Figure 14: Influence of the artificial parameter ϵ on collision time and volume change after the collision.

The numerical investigations of merging and impacting dynamics of droplets are still being actively studied, in which more physical mechanisms should be considered. For example, the merging of droplets depends on the attractive forces and the draining speed of the fluids between the coalescing parts. The attractive forces are usually not included in the continuum description and the draining process could be considered as a pipe flow problem on a smaller scale. Including these mechanisms with very small scales would complicate the computational model and significantly increase the computational cost. To establish computationally tractable models and numerical methods is still at the core of the future study.

5. Conclusion

In this work, we developed a hybrid second-order preserving numerical method to simulate the moving contact line problems with topological changes. The problem was modeled by the two-phase incompressible Navier-Stokes equations with the Navier-slip condition and the contact angle condition. We decoupled the solutions of the velocity field and the interface kinematics in an alternating way. Based on the pressure Poisson equation formulation, we derived the jump conditions in the x- and y-directions to calculate the correction terms, which were used in the immersed interface method to solve for the velocity field. Once the velocity field was obtained, we solved for the motion of the interface by a variational formulation of the kinematic condition and the contact angle condition, where the parametric FEM was employed.

To simulate the problems with the occurrence of coalescence and breakup, we utilized Lagrangian information and introduced a spatial indicator parameter to detect topological change events. Due to the long-time equidistribution property of interface markers, no extra work is needed for re-distributing the markers. Numerical simulations showed that the interfaces and the contact lines are second-order accurate before and after a topological change. A series of simulations were presented to study droplet merging and impact dynamics, and the results showed the capability of the proposed method in capturing topological changes.

In the current work, we only considered constant density in the incompressible Navier-Stokes equations. In more realistic multiphase flow problems, the densities of different fluids are typically different and the jumps in the density variable across their interfaces usually arise. However, the discontinuity in the density would give rise to a nonzero contribution from momentum terms (cf. Equation (17)), which leads to more complex jump conditions. This will be our future concern.

In the aspect of numerical analysis, rigorous proof of second-order convergence for our hybrid method also demands intensive study. One can find the convergence analysis of the immersed interface method for multiphase Stokes flow with a fixed interface [59], and that of the parametric FEM for mean curvature flow [60]. To the best of the authors' knowledge, little analysis has been done for the hybrid method, even in the case of multiphase flow without moving contact lines. The inclusion of contact line dynamics would rather complicate the model and introduce multiscale issues, which make it very challenging for the design of efficient numerical methods and the corresponding analysis. This together with the more sophisticated techniques for handling topological changes will be the topics of future work.

Acknowledgments

The work of Zhilin Li is partially supported by a Simons grant (No. 633724). The work of Zhen Zhang is partially supported by the NSFC grant (NO. 12071207), the Natural Science Foundation of Guangdong Province (2021A1515010359), and the Guangdong Provincial Key Laboratory of Computational Science and Material Design (No. 2019B030301001). The research of Zhiwen Zhang is supported by Hong Kong RGC grant (Project 17307921), the National Natural Science Foundation of China (Project 12171406), and Seed Funding for Strategic Interdisciplinary Research Scheme 2021/22 (HKU).

Authors' Contributions

S. Chai and Z. Zhang developed the numerical methods. S. Chai did the simulations. Z. Li, Z. Zhang and ZW. Zhang designed and coordinated the project. All participated in the preparation

of the manuscript. All authors gave final approval for publication.

Appendix A. Additional jump conditions for the PPE formulation

Based on the jump conditions (23), we can derive the jumps $\left[\frac{\partial^2 \mathbf{u}}{\partial n^2}\right]$ and $\left[\frac{\partial^2 p}{\partial n^2}\right]$ in the case of continuous viscosity, by using the PPE formulation (13)-(14) with the incompressibility condition. Substituting the relation

$$\frac{\partial^2 u}{\partial n^2} = \nabla^2 u - \frac{\partial^2 u}{\partial s^2} - \kappa \frac{\partial u}{\partial n}$$

into (14) and then taking the difference of the limits of the resulting equation at the interface from each side Ω_i, we have the relation

$$\left[\frac{\partial^2 u}{\partial n^2}\right] = Re\left[\frac{\partial p}{\partial x}\right] - \left[\frac{\partial^2 u}{\partial s^2}\right] - \kappa\left[\frac{\partial u}{\partial n}\right],$$

where the equality (16) is used. On the right-hand side of the above equality, the second and the third term vanish due to (23), while the first term can also be calculated from (23) by local coordinate transformation. As a result, we can express the jump $\left[\frac{\partial^2 u}{\partial n^2}\right]$ as

$$\left[\frac{\partial^2 u}{\partial n^2}\right] = Re\left[\frac{\partial p}{\partial x}\right]. \tag{A.1}$$

Similarly, we also have

$$\left[\frac{\partial^2 v}{\partial n^2}\right] = Re\left[\frac{\partial p}{\partial y}\right]. \tag{A.2}$$

Based on (13), we derive the jump in the second-order derivative of p in the same way and obtain that

$$\left[\frac{\partial^2 p}{\partial n^2}\right] = -\rho\left[\nabla\cdot(\mathbf{u}\cdot\nabla\mathbf{u})\right] - \left[\frac{\partial^2 p}{\partial s^2}\right] - \kappa\left[\frac{\partial p}{\partial n}\right].$$

Direct calculations lead to

$$\left[\nabla\cdot(\mathbf{u}\cdot\nabla\mathbf{u})\right] = \left[\nabla\mathbf{u} : (\nabla\mathbf{u})^\top\right] + \left[\mathbf{u}\cdot\nabla(\nabla\cdot\mathbf{u})\right] = 0, \tag{A.3}$$

where : denotes the Frobenius inner product. Here we have used the incompressibility condition, and simplified the first term based on the following formula for the jump:

$$[a\cdot b] = a^-\cdot[b] + b^-\cdot[a] + [a]\cdot[b] = a^+\cdot[b] + b^+\cdot[a] - [a]\cdot[b],$$

where $(\cdot)^-$ and $(\cdot)^+$ denote the limits at the interface approaching from Ω_1 and Ω_2 respectively [61]. By using (23), is further simplified as

$$\left[\frac{\partial^2 p}{\partial n^2}\right] = -\left[\frac{\partial^2 p}{\partial s^2}\right]. \tag{A.4}$$

Finally, based on (23) and (24), we can easily express all these jumps in terms of the x- and y-partial derivatives. For example,

$$\left[\frac{\partial^2 p}{\partial x^2}\right] = \cos^2\psi\left[\frac{\partial^2 p}{\partial n^2}\right] - 2\sin\psi\cos\psi\frac{\partial}{\partial s}\left[\frac{\partial p}{\partial n}\right] + \sin^2\psi\left[\frac{\partial^2 p}{\partial s^2}\right] = \frac{1}{We}\left(-\cos 2\psi\frac{\partial^2\kappa}{\partial s^2}\right).$$

References

[1] G. Korotcenkov, Handbook of Gas Sensor Materials: Properties, Advantages and Shortcomings for Applications Volume 1: Conventional Approaches, Springer, 2013.

[2] B. J. De Gans, P. C. Duineveld, U. S. Schubert, Inkjet printing of polymers: state of the art and future developments, Advanced Materials 16 (3) (2004) 203–213.

[3] C. Huh, L. E. Scriven, Hydrodynamic model of steady movement of a solid/liquid/fluid contact line, Journal of Colloid and Interface Science 35 (1) (1971) 85–101.

[4] E. B. Dussan V, S. H. Davis, On the motion of a fluid-fluid interface along a solid surface, Journal of Fluid Mechanics 65 (1) (1974) 71–95.

[5] R. Cox, The dynamics of the spreading of liquids on a solid surface. Part 1. Viscous flow, Journal of Fluid Mechanics 168 (1986) 169–194.

[6] M.-Y. Zhou, P. Sheng, Dynamics of immiscible-fluid displacement in a capillary tube, Physical Review Letters 64 (8) (1990) 882.

[7] F. Brochard-Wyart, P. G. De Gennes, Dynamics of partial wetting, Advances in Colloid and Interface Science 39 (1992) 1–11.

[8] T. Qian, X.-P. Wang, P. Sheng, Molecular scale contact line hydrodynamics of immiscible flows, Physical Review E 68 (1) (2003) 016306.

[9] W. Ren, W. E, Boundary conditions for the moving contact line problem, Physics of Fluids 19 (2) (2007) 022101.

[10] P. Yue, C. Zhou, J. J. Feng, Sharp-interface limit of the Cahn-Hilliard model for moving contact lines, Journal of Fluid Mechanics 645 (2010) 279.

[11] T. Young, An essay on the cohesion of fluids, Philosophical Transactions of the Royal Society of London (95) (1805) 65–87.

[12] J.-F. Gerbeau, T. Lelievre, Generalized Navier boundary condition and geometric conservation law for surface tension, Computer Methods in Applied Mechanics and Engineering 198 (5-8) (2009) 644–656.

[13] S. Ganesan, L. Tobiska, Arbitrary Lagrangian–Eulerian finite-element method for computation of two-phase flows with soluble surfactants, Journal of Computational Physics 231 (9) (2012) 3685–3702.

[14] T.-P. Fries, T. Belytschko, The extended/generalized finite element method: an overview of the method and its applications, International Journal for Numerical Methods in Engineering 84 (3) (2010) 253–304.

[15] J. Chessa, T. Belytschko, An extended finite element method for two-phase fluids, Journal of Applied Mechanics 70 (1) (2003) 10–17.

[16] Z. Li, The immersed interface method using a finite element formulation, Applied Numerical Mathematics 27 (3) (1998) 253–267.

[17] Z. Li, T. Lin, X. Wu, New Cartesian grid methods for interface problems using the finite element formulation, Numerische Mathematik 96 (1) (2003) 61–98.

[18] C. S. Peskin, The immersed boundary method, Acta Numerica 11 (2002) 479–517.

[19] Y. Kim, M.-C. Lai, C. S. Peskin, Numerical simulations of two-dimensional foam by the immersed boundary method, Journal of Computational Physics 229 (13) (2010) 5194–5207.

[20] R. J. Leveque, Z. Li, The immersed interface method for elliptic equations with discontinuous coefficients and singular sources, SIAM Journal on Numerical Analysis 31 (4) (1994) 1019–1044.

[21] R. J. LeVeque, Z. Li, Immersed interface methods for Stokes flow with elastic boundaries or surface tension, SIAM Journal on Scientific Computing 18 (3) (1997) 709–735.

[22] Z. Li, M.-C. Lai, The immersed interface method for the Navier–Stokes equations with singular forces, Journal of Computational Physics 171 (2) (2001) 822–842.

[23] Z. Li, M.-C. Lai, G. He, H. Zhao, An augmented method for free boundary problems with moving contact lines, Computers & fluids 39 (6) (2010) 1033–1040.

[24] R. P. Fedkiw, T. Aslam, B. Merriman, S. Osher, A non-oscillatory Eulerian approach to interfaces in multimaterial flows (the ghost fluid method), Journal of Computational Physics 152 (2) (1999) 457–492.

[25] A. Mayo, The fast solution of Poisson's and the biharmonic equations on irregular regions, SIAM Journal on Numerical Analysis 21 (2) (1984) 285–299.

[26] I. B. Bazhlekov, P. D. Anderson, H. E. Meijer, Numerical investigation of the effect of insoluble surfactants on drop deformation and breakup in simple shear flow, Journal of Colloid and Interface Science 298 (1) (2006) 369–394.

[27] S. A. Sauter, C. Schwab, Boundary Element Methods, Springer, 2011.

[28] P. D. Spelt, A level-set approach for simulations of flows with multiple moving contact lines with hysteresis, Journal of Computational physics 207 (2) (2005) 389–404.

[29] J.-J. Xu, Z. Li, J. Lowengrub, H. Zhao, A level-set method for interfacial flows with surfactant, Journal of Computational Physics 212 (2) (2006) 590–616.

[30] J.-J. Xu, W. Ren, A level-set method for two-phase flows with moving contact line and insoluble surfactant, Journal of Computational Physics 263 (2014) 71–90.

[31] M. Renardy, Y. Renardy, J. Li, Numerical simulation of moving contact line problems using a volume-of-fluid method, Journal of Computational Physics 171 (1) (2001) 243–263.
[32] C. Josserand, L. Lemoyne, R. Troeger, S. Zaleski, Droplet impact on a dry surface: triggering the splash with a small obstacle, Journal of Fluid Mechanics 524 (2005) 47.
[33] D. Legendre, M. Maglio, Comparison between numerical models for the simulation of moving contact lines, Computers & Fluids 113 (2015) 2–13.
[34] D. M. Anderson, G. B. McFadden, A. A. Wheeler, Diffuse-interface methods in fluid mechanics, Annual Review of Fluid Mechanics 30 (1) (1998) 139–165.
[35] G. Tryggvason, B. Bunner, A. Esmaeeli, D. Juric, N. Al-Rawahi, W. Tauber, J. Han, S. Nas, Y.-J. Jan, A front-tracking method for the computations of multiphase flow, Journal of Computational Physics 169 (2) (2001) 708–759.
[36] J. Glimm, J. W. Grove, X. L. Li, D. C. Tan, Robust computational algorithms for dynamic interface tracking in three dimensions, SIAM Journal on Scientific Computing 21 (6) (2000) 2240–2256.
[37] M. Muradoglu, S. Tasoglu, A front-tracking method for computational modeling of impact and spreading of viscous droplets on solid walls, Computers & Fluids 39 (4) (2010) 615–625.
[38] Q. Zhang, A. Fogelson, MARS: an analytic framework of interface tracking via mapping and adjusting regular semialgebraic sets, SIAM Journal on Numerical Analysis 54 (2) (2016) 530–560.
[39] S. Leung, H. Zhao, A grid based particle method for moving interface problems, Journal of Computational Physics 228 (8) (2009) 2993–3024.
[40] Q. Zhang, On a family of unsplit advection algorithms for volume-of-fluid methods, SIAM Journal on Numerical Analysis 51 (5) (2013) 2822–2850.
[41] J. W. Barrett, H. Garcke, R. Nürnberg, A parametric finite element method for fourth order geometric evolution equations, Journal of Computational Physics 222 (1) (2007) 441–467.
[42] J. W. Barrett, H. Garcke, R. Nürnberg, On the variational approximation of combined second and fourth order geometric evolution equations, SIAM Journal on Scientific Computing 29 (3) (2007) 1006–1041.
[43] W. Bao, W. Jiang, Y. Wang, Q. Zhao, A parametric finite element method for solid-state dewetting problems with anisotropic surface energies, Journal of Computational Physics 330 (2017) 380–400.
[44] Q. Zhao, W. Jiang, W. Bao, A parametric finite element method for solid-state dewetting problems in three dimensions, SIAM Journal on Scientific Computing 42 (1) (2020) B327–B352.
[45] Q. Zhao, W. Ren, An energy-stable finite element method for the simulation of moving contact lines in two-phase flows, Journal of Computational Physics 417 (2020) 109582.
[46] S. Chai, Z. Zhang, Z. Zhang, A second order accuracy preserving method for moving contact lines with Stokes flow, Journal of Computational Physics 445 (2021) 110607.
[47] A. J. Chorin, Numerical solution of the Navier-Stokes equations, Mathematics of Computation 22 (104) (1968) 745–762.
[48] D. L. Brown, R. Cortez, M. L. Minion, Accurate projection methods for the incompressible Navier–Stokes equations, Journal of Computational Physics 168 (2) (2001) 464–499.
[49] P. M. Gresho, R. L. Sani, On pressure boundary conditions for the incompressible Navier-Stokes equations, International Journal for Numerical Methods in Fluids 7 (10) (1987) 1111–1145.
[50] H. Johnston, J.-G. Liu, Accurate, stable and efficient Navier–Stokes solvers based on explicit treatment of the pressure term, Journal of Computational Physics 199 (1) (2004) 221–259.
[51] Z. Li, M.-C. Lai, X. Peng, Z. Zhang, A least squares augmented immersed interface method for solving Navier–Stokes and Darcy coupling equations, Computers & Fluids 167 (2018) 384–399.
[52] H. Johnston, J.-G. Liu, Finite difference schemes for incompressible flow based on local pressure boundary conditions, Journal of Computational Physics 180 (1) (2002) 120–154.
[53] Z. Li, K. Ito, The Immersed Interface Method: Numerical Solutions of PDEs Involving Interfaces and Irregular Domains, SIAM, 2006.
[54] P. M. Gresho, Some current CFD issues relevant to the incompressible Navier-Stokes equations, Computer Methods in Applied Mechanics and Engineering 87 (2-3) (1991) 201–252.
[55] D. Enright, R. Fedkiw, J. Ferziger, I. Mitchell, A hybrid particle level set method for improved interface capturing, Journal of Computational Physics 183 (1) (2002) 83–116.
[56] J. Li, Macroscopic model for head-on binary droplet collisions in a gaseous medium, Physical Review Letters 117 (21) (2016) 214502.
[57] L. Wang, H.-B. Huang, X.-Y. Lu, Scheme for contact angle and its hysteresis in a multiphase lattice Boltzmann method, Physical Review E 87 (1) (2013) 013301.
[58] Y. J. Jiang, A. Umemura, C. K. Law, An experimental investigation on the collision behaviour of hydrocarbon droplets, Journal of Fluid Mechanics 234 (1992) 171–190.
[59] R. Hu, Z. Li, Error analysis of the immersed interface method for Stokes equations with an interface, Applied Mathematics Letters 83 (2018) 207–211.

[60] B. Li, Convergence of Dziuk's linearly implicit parametric finite element method for curve shortening flow, SIAM Journal on Numerical Analysis 58 (4) (2020) 2315–2333.
[61] S. Xu, Z. J. Wang, An immersed interface method for simulating the interaction of a fluid with moving boundaries, Journal of Computational Physics 216 (2) (2006) 454–493.